

REPORT DOCUMENTATION PAGE			Form Approved OMB NO. 0704-0188		
<p>The public reporting burden for this collection of information is estimated to average 1 hour per response, including the time for reviewing instructions, searching existing data sources, gathering and maintaining the data needed, and completing and reviewing the collection of information. Send comments regarding this burden estimate or any other aspect of this collection of information, including suggestions for reducing this burden, to Washington Headquarters Services, Directorate for Information Operations and Reports, 1215 Jefferson Davis Highway, Suite 1204, Arlington VA, 22202-4302. Respondents should be aware that notwithstanding any other provision of law, no person shall be subject to any penalty for failing to comply with a collection of information if it does not display a currently valid OMB control number.</p> <p>PLEASE DO NOT RETURN YOUR FORM TO THE ABOVE ADDRESS.</p>					
1. REPORT DATE (DD-MM-YYYY) 17-08-2015		2. REPORT TYPE Final Report		3. DATES COVERED (From - To) 18-Aug-2014 - 17-May-2015	
4. TITLE AND SUBTITLE Final Report: STIR: Multi-scale Texturing of Metallic Surfaces for High Performance Military Systems			5a. CONTRACT NUMBER W911NF-14-1-0566		
			5b. GRANT NUMBER		
			5c. PROGRAM ELEMENT NUMBER 611102		
6. AUTHORS Christopher Saldana, Robert C. Voigt			5d. PROJECT NUMBER		
			5e. TASK NUMBER		
			5f. WORK UNIT NUMBER		
7. PERFORMING ORGANIZATION NAMES AND ADDRESSES Pennsylvania State University Office of Sponsored Programs 110 Technology Center Building University Park, PA 16802 -7000			8. PERFORMING ORGANIZATION REPORT NUMBER		
9. SPONSORING/MONITORING AGENCY NAME(S) AND ADDRESS (ES) U.S. Army Research Office P.O. Box 12211 Research Triangle Park, NC 27709-2211			10. SPONSOR/MONITOR'S ACRONYM(S) ARO		
			11. SPONSOR/MONITOR'S REPORT NUMBER(S) 66086-MS-II.5		
12. DISTRIBUTION AVAILABILITY STATEMENT Approved for Public Release; Distribution Unlimited					
13. SUPPLEMENTARY NOTES The views, opinions and/or findings contained in this report are those of the author(s) and should not be construed as an official Department of the Army position, policy or decision, unless so designated by other documentation.					
14. ABSTRACT The focus of the present study was on establishing principles to support multi-scale surface texturing of metallic components for use in military performance applications. In this regard, two different surface texturing/modification methods were considered: Surface Severe Plastic Deformation (S2PD) and Modulation-Assisted Texturing (MAT). For S2PD, the effects of processing parameters on the resulting subsurface deformation field in terms of both mechanics and microstructure (e.g., microstructure, texture) were quantified for a unit model process as well as for an aggregate level strain induced surface modification configuration. For MAT, the effects					
15. SUBJECT TERMS Surface Modification, Surface Processing, Surface Severe Plastic Deformation, Subsurface Texture Control					
16. SECURITY CLASSIFICATION OF:			17. LIMITATION OF ABSTRACT UU	15. NUMBER OF PAGES	19a. NAME OF RESPONSIBLE PERSON Christopher Saldana
a. REPORT UU	b. ABSTRACT UU	c. THIS PAGE UU			19b. TELEPHONE NUMBER 814-865-7397

Report Title

Final Report: STIR: Multi-scale Texturing of Metallic Surfaces for High Performance Military Systems

ABSTRACT

The focus of the present study was on establishing principles to support multi-scale surface texturing of metallic components for use in military performance applications. In this regard, two different surface texturing/modification methods were considered: Surface Severe Plastic Deformation (S2PD) and Modulation-Assisted Texturing (MAT). For S2PD, the effects of processing parameters on the resulting subsurface deformation field in terms of both mechanics and microstructure (e.g., microstructure, texture) were quantified for a unit model process as well as for an aggregate-level, strain-induced surface modification configuration. For MAT, the effects of surface texture form (e.g., micro-scale topography) on surface integrity measures and tribological wear performance were quantified. The ensuing results are useful as a preliminary step toward realizing a hybrid model-based processing framework for designing multi-functional surfaces with significantly enhanced mission-specific performance capabilities.

Enter List of papers submitted or published that acknowledge ARO support from the start of the project to the date of this printing. List the papers, including journal references, in the following categories:

(a) Papers published in peer-reviewed journals (N/A for none)

<u>Received</u>	<u>Paper</u>
-----------------	--------------

TOTAL:

Number of Papers published in peer-reviewed journals:

(b) Papers published in non-peer-reviewed journals (N/A for none)

<u>Received</u>	<u>Paper</u>
-----------------	--------------

TOTAL:

Number of Papers published in non peer-reviewed journals:

(c) Presentations

Number of Presentations: 0.00

Non Peer-Reviewed Conference Proceeding publications (other than abstracts):

Received

Paper

TOTAL:

Number of Non Peer-Reviewed Conference Proceeding publications (other than abstracts):

Peer-Reviewed Conference Proceeding publications (other than abstracts):

Received

Paper

08/17/2015	3.00	Saurabh Basu, Zhiyu Wang, Christopher Saldana. CRYSTALLOGRAPHIC TEXTURES PRODUCED DURING SAND BLASTING, ASME 2015 International Manufacturing Science and Engineering. 08-JUN-15, . : ,
08/17/2015	4.00	Zhiyu Wang, Saurabh Basu, Christopher Saldana. SUBSURFACE DEFORMATION IN SURFACE MECHANICAL ATTRITION PROCESSES, ASME 2015 International Manufacturing Science and Engineering Conference. 08-JUN-15, . : ,

TOTAL: 2

Number of Peer-Reviewed Conference Proceeding publications (other than abstracts):

(d) Manuscripts

Received

Paper

08/17/2015	1.00	Saurabh Basu, Zhiyu Wang, Christopher Saldana. Deformation heterogeneity and texture in surface severe plastic deformation of copper, Submitted for publication (07 2015)
08/17/2015	2.00	D. Sebastian, S. Basu, J. B. Mann, P. Iglesias, C. Saldana, R. Gandhi . Surfaces by Vibration/Modulation-Assisted Texturing for Tribological Applications, Submitted for publication (08 2015)

TOTAL: 2

Number of Manuscripts:

Books

Received Book

TOTAL:

Received Book Chapter

TOTAL:

Patents Submitted

Patents Awarded

Awards

Graduate Students

<u>NAME</u>	<u>PERCENT SUPPORTED</u>	Discipline
Zhiyu Wang	0.00	
Ryan Liu	0.00	
FTE Equivalent:	0.00	
Total Number:	2	

Names of Post Doctorates

<u>NAME</u>	<u>PERCENT SUPPORTED</u>
Saurabh Basu	1.00
FTE Equivalent:	1.00
Total Number:	1

Names of Faculty Supported

<u>NAME</u>	<u>PERCENT SUPPORTED</u>	National Academy Member
Christopher Saldana	0.00	
Robert C. Voigt	0.00	
FTE Equivalent:	0.00	
Total Number:	2	

Names of Under Graduate students supported

<u>NAME</u>	<u>PERCENT SUPPORTED</u>
FTE Equivalent:	
Total Number:	

Student Metrics

This section only applies to graduating undergraduates supported by this agreement in this reporting period

The number of undergraduates funded by this agreement who graduated during this period: 0.00

The number of undergraduates funded by this agreement who graduated during this period with a degree in science, mathematics, engineering, or technology fields:..... 0.00

The number of undergraduates funded by your agreement who graduated during this period and will continue to pursue a graduate or Ph.D. degree in science, mathematics, engineering, or technology fields:..... 0.00

Number of graduating undergraduates who achieved a 3.5 GPA to 4.0 (4.0 max scale):..... 0.00

Number of graduating undergraduates funded by a DoD funded Center of Excellence grant for Education, Research and Engineering:..... 0.00

The number of undergraduates funded by your agreement who graduated during this period and intend to work for the Department of Defense 0.00

The number of undergraduates funded by your agreement who graduated during this period and will receive scholarships or fellowships for further studies in science, mathematics, engineering or technology fields:..... 0.00

Names of Personnel receiving masters degrees

<u>NAME</u>
Ryan Liu
Total Number:

Names of personnel receiving PHDs

<u>NAME</u>
Total Number:

Names of other research staff

<u>NAME</u>	<u>PERCENT SUPPORTED</u>
FTE Equivalent:	
Total Number:	

Sub Contractors (DD882)

1 a. Georgia Institute of Technology

1 b. 225 NORTH AVENUE

ATLANTA GA 303320357

Sub Contractor Numbers (c):

Patent Clause Number (d-1):

Patent Date (d-2):

Work Description (e):

Sub Contract Award Date (f-1):

Sub Contract Est Completion Date(f-2):

1 a. Georgia Institute of Technology

1 b. 225 NORTH AVENUE

ATLANTA GA 303320357

Sub Contractor Numbers (c):

Patent Clause Number (d-1):

Patent Date (d-2):

Work Description (e):

Sub Contract Award Date (f-1):

Sub Contract Est Completion Date(f-2):

Inventions (DD882)

Scientific Progress

Technology Transfer

See Attachment

Final Technical Report

STIR: Multi-Scale Texturing of Metallic Surfaces for High Performance Military Systems

University Project Team:

C. Saldana (Georgia Tech), christopher.saldana@me.gatech.edu, 404.385.3735

R. Voigt (Pennsylvania State University), rcv2@engr.psu.edu, 814.863.7290

University Administrative Contacts:

A. Eisenhower (Pennsylvania State University), alm25@psu.edu, 814.865.6185

M. Wan (Georgia Tech), millie.wan@me.gatech.edu, 404.894.7149

ARO Point of Contact: Dr. David Stepp

Project End Date: 17 May 2015

Technical Report Date: 15 June 2015

1. Foreword

The following document provides a final progress report for the work completed under a Short Term Innovative Research (STIR) award from the US Army Research Office to a team from The Pennsylvania State University (PSU) and Georgia Institute of Technology (GT). The PIs for this project were C. Saldana (GT) and R. Voigt (PSU). The STIR project was initiated at PSU with C. Saldana as PI, whom subsequently transferred primary employment to GT during the contracting period. The project was then subcontracted to GT by PSU.

2. Table of Contents

Foreword	2
List of Appendices, Illustrations, Tables	2
Statement of Problem Studied	2
Summary of Important Results	3
Future Studies and Implementation on Continuous Processing Systems	14
Publications Resulting From this Project	15
Bibliography	15

3. List of Appendices, Illustrations and Tables

- Figure 1. *In-situ* characterization of material flow during surface deformation.
- Figure 2. Orientation imaging microscopy underneath unit surface deformation test.
- Figure 3. Empirical and simulated crystallographic textures corresponding to subsurface regions after surface indentation.
- Figure 4. Simulated response of material to a single surface impact.
- Figure 5. Numerically obtained strain profiles under the surface deformed by SMAT.
- Figure 6. Empirical and simulated (111), (022) pole figures from initial and post-SMAT samples.
- Figure 7. Empirical and simulated orientation distribution functions.
- Figure 8. Schematic showing tooling configuration to produce textured surfaces.
- Figure 9. Tool motions in plunging-type texturing and sliding-type texturing.
- Figure 10. Experimental machining setup and ball-on-flat wear test configuration.
- Table 1. Experimental surface texturing conditions and measurements for wear tests.
- Figure 11. Surfaces created by plunging-type texturing.
- Figure 12. Wear factor measurements and wear track profiles for control surface samples and textured surface samples.
- Figure 13. Subsurface microstructure and texture in topographical surface texturing.

4. Statement of the Problem Studied

The focus of the present study was on establishing principles to support multi-scale surface texturing of metallic components for use in military performance applications. In this regard, two different surface texturing/modification methods were considered: Surface Severe Plastic Deformation (S^2PD) and Modulation-Assisted Texturing (MAT). For S^2PD , the effects of processing parameters on the resulting subsurface deformation field in terms of both mechanics and microstructure (e.g., microstructure, texture) were quantified for a unit model process as well as for an aggregate-level, strain-induced surface modification configuration. For MAT, the effects of surface texture form (e.g., micro-scale topography) on surface integrity measures and tribological wear performance were quantified. The ensuing results are useful as a preliminary step toward realizing a hybrid model-based processing framework for designing multi-functional surfaces with significantly enhanced mission-specific performance capabilities.

5. Summary of the Most Important Results

The primary project results are summarized below in terms of experimental and modeling results associated with the surface severe plastic deformation and controlled surface texturing methods investigated.

5.1 Surface Severe Plastic Deformation (S^2PD)

In the present project, the evolution of microstructure and crystallographic texture during S^2PD in SMAT were investigated. As the microstructure created during SMAT is a consequence of the coupled effect of multiple surface impacts/indentations, insights were assembled from elucidating the mechanics and microstructure evolution in a unit surface indentation process (e.g., unit model mechanics) and using these models to establish effects in a scaled configuration (e.g., S^2PD processing).

5.1.1 Unit Model Mechanics

Digital Image Correlation (DIC) was used to characterize material flow during surface indentation. For this, the face of the workpiece (plane Y-Z in Fig. 1) exposed through the tempered glass window was illuminated during indentation using a bright light source, which resulted in a concentrated speckle pattern on its surface. Material flow was recorded in a sequence of digital images captured using a high-speed camera. Subsequently, movement of these speckles due to deformation imposed during indentation was delineated using image correlation algorithms. Subroutines were thereafter implemented to extract several deformation parameters including strain rate fields, strain fields and rotation fields. To do this, a grid was defined in the region of interest under the indenter. Subsequently, path lines followed by each point in the grid were extracted and deformation experienced by the corresponding point in the grid were integrated along the path line. In this manner, deformation histories of different material points under the impacting media were characterized. The computational routines were written in-house using Matlab [1]. The deformation histories were coupled with the Visco-Plastic Self-Consistent polycrystal (VPSC) framework to simulate evolution of crystallographic textures [2].

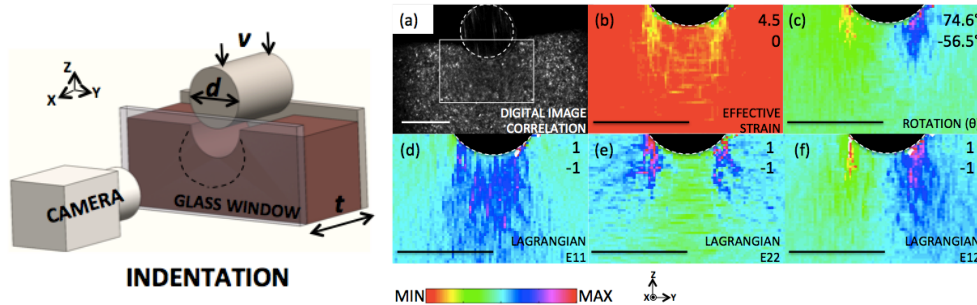


Figure 1. *In-situ* characterization of material flow during surface deformation. Characterization of (a) deformation fields to produce: (b) effective strain, (c) rotation and (d)-(f) Lagrangian strain components.

Orientation imaging microscopy (OIM) of deformed samples was performed using electron backscatter diffraction (EBSD). Specimens were prepared by mounting deformed samples in epoxy, followed by mechanical polishing to 0.04 μm finishes. Final mechanical polishing was performed using colloidal silica for longer periods for enhancing indexing. Subsequently, samples were also polished with a Hitachi 4000 plus ion beam polisher for 5 mins. Scan step sizes between 0.1 μm -1 μm were used. Larger scan step sizes facilitated quick collection of statistically significant data for studying crystallographic textures. Beam diameter was set at 150 nm and accelerating voltage was set at 20 KV. Analysis of crystallographic textures extracted from EBSD micro-graphs was performed using MTEX software. Inverse pole figures (IPFs) illustrating empirically observed evolution of microstructure at different locations under the indenter are

shown in Fig. 2. The grains exhibit a pancaked shape closer to the indenter-workpiece interface due to shear imposed (region I). However, this effect decays with strain away from the indenter, as evidenced from near uniaxial grain morphologies observed in these regions (Fig. 2, regions II and III).

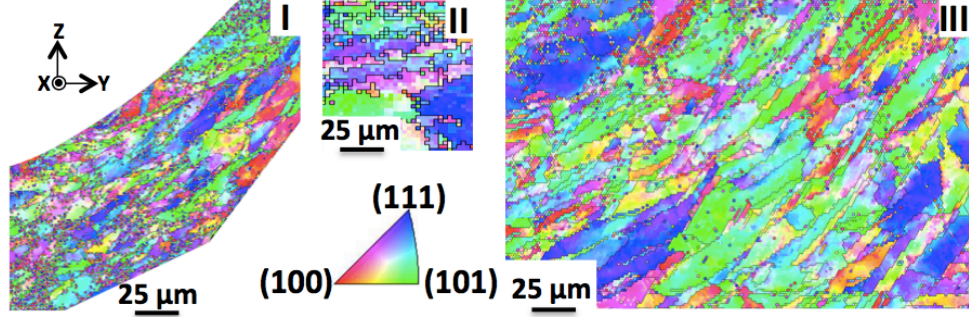


Figure 2. Orientation imaging microscopy underneath unit surface deformation test. Three regions (I, II and III) were chosen for performing OIM. Refer inverse pole figure inset for color code.

Crystallographic textures comprising orientation distribution functions (ODFs) and pole figures (Fig. 3) were extracted from these IPFs by discrete binning of the orientations. Significant differences between crystallographic textures extracted from the three different locations were seen, owing to the heterogeneous deformation under the indenter manifesting through different strain tensor components (Fig. 1). The strain tensor components were calculated using $\underline{E} = \frac{1}{2}(\underline{F}^T \cdot \underline{F} - \underline{I})$ where \underline{I} is the identity tensor. For instance, crystallographic textures in region I (Fig. 3) exhibit a dominant simple shear character featuring concentrations along fibers reminiscent of the f_1 , f_2 and f_3 fibers conventionally seen in simple shear deformation geometries [3]. The Lagrangian strain tensor components in this region were $E_{11} = 0.1$, $E_{22} = -0.1$ and $E_{12} = 0.9$. E_{11} and E_{22} refer to the horizontal E_{YY} and vertical E_{ZZ} Lagrangian strain components, respectively. On the other hand, crystallographic textures in, region II (Fig. 3) exhibit a uniaxial tension character, with the tensile axis oriented along the horizontal (Y) direction [4]. This is due to the dominant uniaxial strain component in region II with $E_{11} = 0.2$, $E_{22} = -0.2$ and $E_{12} = 0.01$.

Evolution of crystallographic textures during indentation was modeled using the VPSC framework. For this, the deformation histories were obtained from *in situ* DIC based characterization of the deformation zone during indentation. Pre-deformation crystallographic textures were characterized by OIM using EBSD and revealed lack of preferred orientations (e.g., random crystallographic textures), as in Fig. 3. Hence, the pre-deformation discretized ODFs for input to the VPSC framework were produced by sampling from uniformly distributed orientation space. Numerically simulated crystallographic textures in surface indentation are shown in Fig. 3. Here, parameters of the VPSC framework were tuned until a good match between simulated and empirically obtained results was found. It was seen that a grain fragmentation scheme with aspect ratio $R=5$ was adequate for simulating the texture evolution. This scheme of grain fragmentation is in the same vein as mechanics governing geometric dynamic recrystallization, which involves a single long, pancake-shaped grain pinching off into several small grains upon meeting mechanistically defined aspect ratios [5]. While some discrepancies were seen in the maximum intensities of the empirical and simulated crystallographic textures (Fig. 3), the calibrated VPSC frameworks essentially reproduced all qualitative aspects of the post-deformed crystallographic textures. Variations in intensities arose due to large grain sizes manifesting in concentrations in the orientation space.

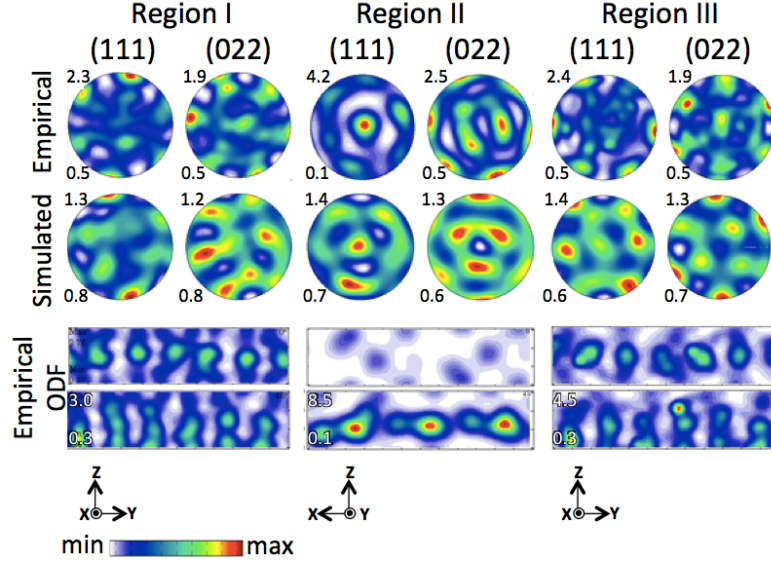


Figure 3. Empirical and simulated crystallographic textures corresponding to subsurface regions after surface indentation. (111) and (022) pole figures as well as $\Phi 2$ sections (0° and 45°) are shown.

5.1.2 S^2PD Processing

Surface mechanical attrition treatment (SMAT) was performed on as-received OFHC Cu (alloy 101: MSC direct, 2.3 mm thick). For SMAT, spherical silica SiO₂ shots (diameter = 200 μ m) were accelerated using a directed blast of air at 90 Psi (0.4 MPa). In this manner, the surface was treated with several hundred impacts oriented perpendicularly with respect to the surface normal (Z axis in Fig. 1) whereby directionality of SMAT was maintained. SMAT was performed for 600 s and 1200 s. The velocity of impact was measured to be approximately 10 m/s by recording the mass flow rate. Numerical simulation was performed using ABAQUS 6.14 as a sequence of impacts, implemented through in-house python subroutines using the scripting interface in ABAQUS. The mechanical state of the workpiece prior to impacts were extracted from the post-deformation state left after the previous impact simulation. Python subroutines were used to achieve this feature whereby the deformation history at the end of an impact is not lost and material response analogous to that in real SMAT comprising a sequence of impacts is simulated. Impacting shots were modeled as spherical elastic bodies with ($d = 200 \mu\text{m}$, $E = 300 \text{ GPa}$, $\nu = 0.21$). The workpiece was modeled as an isothermal body (C3D84 elements) with reduced integration and hourglass control. The iso-thermal state of the workpiece was governed by the diffuse nature of deformation imposed by spatially and temporally discrete impacts across the surface of the workpiece, which prohibit concentrated heat dissipation and temperature rise due to plastic deformation. The workpiece was modeled as a Johnson-Cook material: $\sigma = (A + B\varepsilon^n)(1 + C \log \dot{\varepsilon}/\dot{\varepsilon}_0) \left(1 - \frac{T - T_r}{T_m - T_r}\right)^m$, where $[A, B, C, \dot{\varepsilon}_0, n, m] = [90 \text{ MPa}, 292 \text{ MPa}, 0.025, 1 \text{ s}^{-1}, 0.31, 1.09]$, respectively. Gaussian distributed velocities were assigned to the impacting shots. Post simulation processing was performed to couple data obtained from numerical FEM based simulations with the VPSC framework for simulating evolution of crystallographic textures explicitly. This was done using Python subroutines, whereby displacement undergone by element nodes close to the surface was converted to velocity gradient tensors, which comprises the raw input for the VPSC framework.

Figure 4 shows the response of material to an individual impact $V = -0.5e_x + 0.6e_y - 10e_z \text{ m/s}$. Here e_x , e_y and e_z are unit vectors. Lagrangian strain components reveal a 3D material flow pattern

involving comparable strain components featuring $\max |E_n|$ within the same order of magnitude. Here $|E_n|$ refers to components in the Lagrangian strain tensor \underline{E} . Implications of the 3D nature of the deformation field lie in strain path changes, reversals and spatial strain heterogeneity in the final strain fields. These have further structural and functional manifestations in the resulting product, such as accelerated microstructure refinement during SPD [6, 7]. A maximum effective strain rate $\dot{\epsilon}_{\text{dot}} = 5.3 \times 10^5 \text{ s}^{-1}$ was seen under the impacting shot. Figure 5 shows the numerically simulated strain profiles under the surface treated using SMAT. These curves elucidate representative mean strain profiles obtained from several different locations under the surface. Interestingly, a constant width of material accommodates the strain imposed during SMAT, irrespective of the number of impacts on the surface. Despite a complicated deformation geometry ensuing from the coupled effect of several impacts, the constancy in dimensions of the affected zone is reminiscent similar observations for deformation in burnishing and machining. The simulation was terminated at the end of 850 impacts, at which point a peak effective strain $\epsilon = 1.3$ was seen numerically. The strain field exhibited a near-Gaussian spatial distribution at the end of the simulation, arising from Gaussian distributed velocities of the impacting shots. Additionally, this behavior was coupled with an exponential decay in magnitude under the surface, similar to machining, despite different underlying deformation geometries.

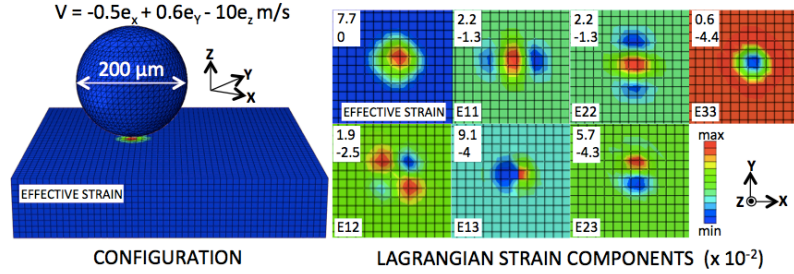


Figure 4. Simulated response of material to a single surface impact. Configuration of the numerical model is shown on the left. Effective and Lagrangian strain tensor field components are shown on the right.

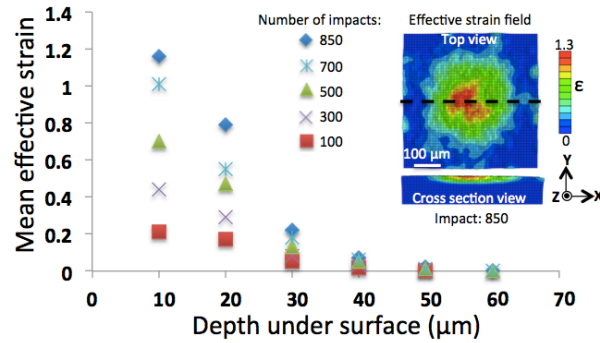


Figure 5. Numerically obtained strain profiles under the surface deformed by SMAT. The inset shows the strain field after 850 impacts and a cross sectional view illustrating the strain profile under the surface.

Characterization of crystallographic textures in as-received and post-SMAT samples was performed in a Panalytical X'Pert pro MRD x-ray diffractometer equipped with a Cu x-ray source, an Eulerian cradle goniometer and a solid state X'celerator detector. Measurements were performed at 45 KV and 40 mA using the $K_{\alpha 1}$ radiation of Cu $\lambda = 1.540598$ angstroms with a scan step size of 5 degrees. For this, the surface perpendicular to the Z direction was exposed to the incident X ray beam. Pole figures corresponding to the first three peaks in Cu (111), (200) and (220) at diffraction angles of 43, 50 and 74 degrees, were measured respectively. The diffraction angles were fine tuned before making each measurement. Post measurement analyses including

pole figure inversion of crystallographic textures were performed using MTEX. Figure 6 shows ODFs and (111) and (022) pole figures of crystallographic textures obtained from surfaces, pre-SMAT and post-SMAT treatments (600 s and 1200 s). Prior to SMAT, the surface exhibits a cube texture with pole figures featuring 2/m symmetry. Upon SMAT, the pole figures assumes 360-degree rotation symmetry about the central axis that corresponds to normal direction with respect to the surface. Additionally, crystallographic textures obtained from 600 s and 1200 s samples show negligible variation with respect to each other suggesting a saturated state of the underlying microstructure with respect to the deformation imposed during SMAT. Such saturated microstructural states are commonly seen during imposition of SPD [8].

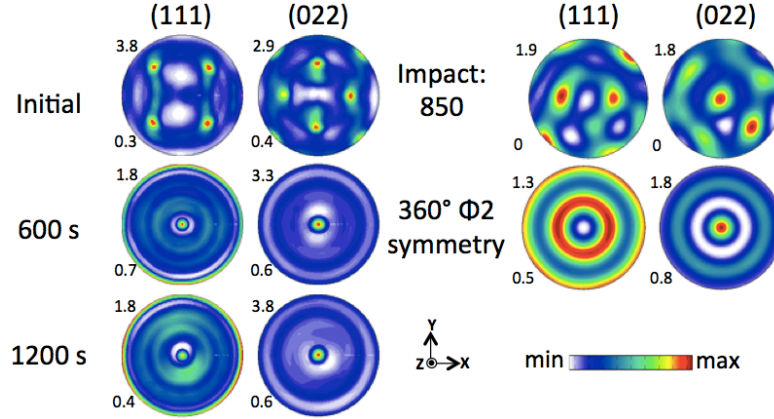


Figure 6. Empirical and simulated (111), (022) pole figures from initial and post-SMAT samples.

Numerically obtained material flow during SMAT was integrated with the VPSC framework explicitly to simulate evolution of crystallographic textures. This was done by extracting the velocity gradient tensors from arbitrarily chosen elements directly under the surface of the numerically simulated workpiece. To this end, elements close to the center of the workpiece exhibiting peak in the Gaussian distributed strain field were chosen. After subsequent post-processing, a compiled deformation history file containing material response data from the impacts was produced and input to the VPSC framework. Here, deformation steps resulting in an incremental effective strain were ignored assuming a purely elastic response. Such events are manifestations of elastic waves from impacts in non-neighboring regions of the arbitrarily chosen element. The starting un-deformed texture which also comprises input to the VPSC framework in a discretized ODF form (i.e., list of grain orientations corresponding to the ODF) was obtained by statistically sampling grains from the empirically measured pre-deformed ODF (Fig. 6).

Simulated crystallographic textures (ODFs, pole figures) are shown in Figs. 6 and 7, respectively, and exhibit qualitative similarity with the empirical counterparts. This is evidenced from the numerically simulated ODFs which exhibit concentrations along fibers featuring $\Phi 2$ symmetry (black arrows in Fig. 7), which correspond to the 360° symmetry of the deformed sample. The location of these fibers was coincident with those obtained empirically through 600 s and 1200 s of SMAT. The discontinuous nature of the fibers obtained numerically is a consequence of spatially discontinuous deformation imposed during the 850 impacts. However, this was not the case empirically owing to the potentially larger number of impacts that result in a more continuous fibers distributed through the orientation space. In order to understand these effects, 360° $\Phi 2$ symmetry was imposed on the numerically obtained crystallographic textures, representative of the numerically obtained saturated state of the workpiece (Fig. 4). Results obtained using this approach coincide well with the empirically obtained crystallographic

textures, as seen in comparison of the pole figures as well as ODFs. On further analysis, it was seen that the crystallographic textures obtained during SMAT share similarities with compression textures, which constitute fibers coincident with those obtained empirically during SMAT. Reasons for this similarity constitute strain path changes involving reversals that negate other Lagrangian strain components that resulted from previous impacts and additively amplify the compression E_{33} component under the surface during SMAT. This elucidation has consequences for realizing process-structure-function frameworks through microstructure engineering using SMAT. The numerical framework essentially enables material flow field prediction as a function of parameters of the SMAT process, which include impacting shot geometry, shot density, velocity and angle of incidence.

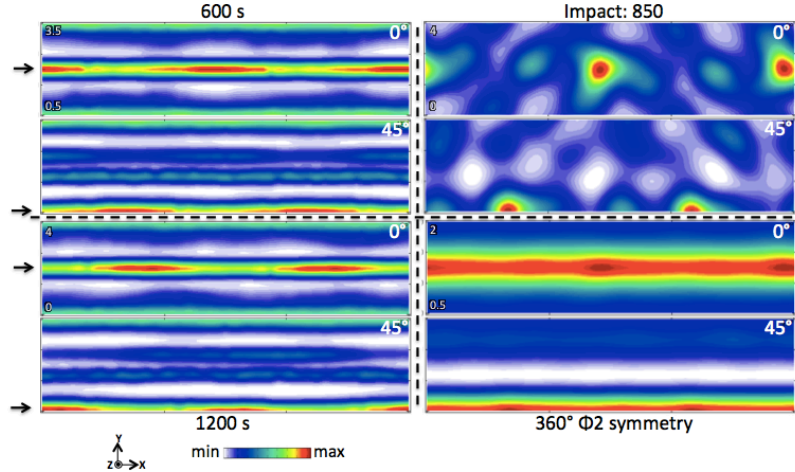


Figure 7. Empirical (600 s, 1200 s) and simulated (850 impacts, 360 Φ 2 symmetry) orientation distribution functions. Black arrows show coincidence of dominant fibers in empirically obtained and numerically simulated samples. Φ 2 sections = 0° and 45° are shown.

Results from these experimental and calibrated numerical investigations can be directly integrated within the expected functional response space in order to optimize surface engineering processes involving SMAT. The framework described is directly relevant to a range of bio-medical implant engineering technologies, especially those involving anisotropically brittle materials, such as Mg alloys. For instance, anisotropy inhibits formability and machinability and prohibits widespread use of Mg alloys in bio-medical applications. As in the above, surface engineering technologies such as SMAT can be used to tune the crystallographic textures of Mg using this framework in order to engineer starting microstructures for engendering higher formability and machinability.

5.2 Multi-Scale Texturing

In the present project, micro-scale textures of controlled size and morphology were generated by control of underlying process parameters in modulation-assisted texturing. Modulation-assisted texturing (MAT) broadly refers to a class of surface generation processes that utilize controlled modulation of the workpiece or tool during conventional machining. Two modulation configurations are considered wherein the superimposed modulation is applied in the direction of the workpiece centerline. The first configuration is that of a facing process with modulation applied in the depth of cut direction, here referred to as plunging-type texturing and depicted in Fig. 8(a). In this configuration, the tool is engaged at a constant depth of cut (d) along the workpiece axis and traverses radially along the end face at a constant feed rate (s_0). The modulation in this case is applied in the depth of cut direction, which causes a periodic change in depth of cut. Depending on the selected parameters, the tool is periodically separated from the workpiece, causing discretization of the chip formation and yielding a periodic texture on the

workpiece face. A second configuration is that of cylindrical turning with modulation applied in the feed direction, here referred to as sliding-type texturing and depicted in Fig. 8(b). In this configuration, the tool is engaged at a constant depth of cut (d) and travels parallel to the axis along the part length at a constant feed rate (s_0). The modulation is applied in the direction of the undeformed chip thickness and the interaction of successive machining passes imparts a periodic micro-scale topography to the surface. Micro-scale depression-type textures (dimples) were generated using these MAT processes and corresponding surface models were developed as a framework for their manufacture. The tribological performance of the dimple-type textures was characterized by ball-on-flat wear testing. The effect of the texturing process on surface and subsurface microstructure was measured using EBSD.

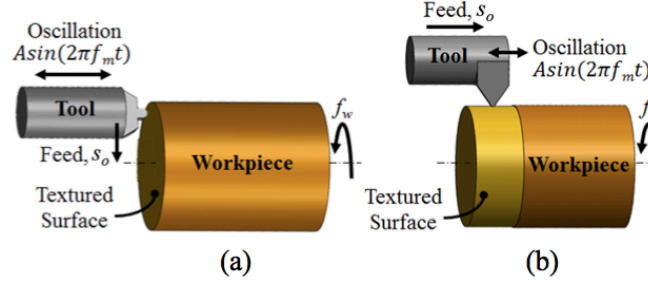


Figure 8. Schematic showing tooling configuration to produce textured surfaces in (a) plunging-type texturing (facing) and (b) sliding-type texturing (turning).

5.2.1 Surface Modeling

A geometric surface model for plunging-type texturing can be determined by considering the interaction of the tool with the work surface. For facing configurations in the absence of superimposed modulation, motion of the texturing tool is restricted to a plane parallel to the work surface and takes the shape of an Archimedean spiral (i.e., $r = a + \theta b$, a and b are constants) as in Eq. (1),

$$r = \frac{s_0 * \theta}{2 * \pi} \quad \text{Eq. (1)}$$

where s_0 is the feed rate, r the radial coordinate and θ the angular coordinate as in Fig. 9(a).

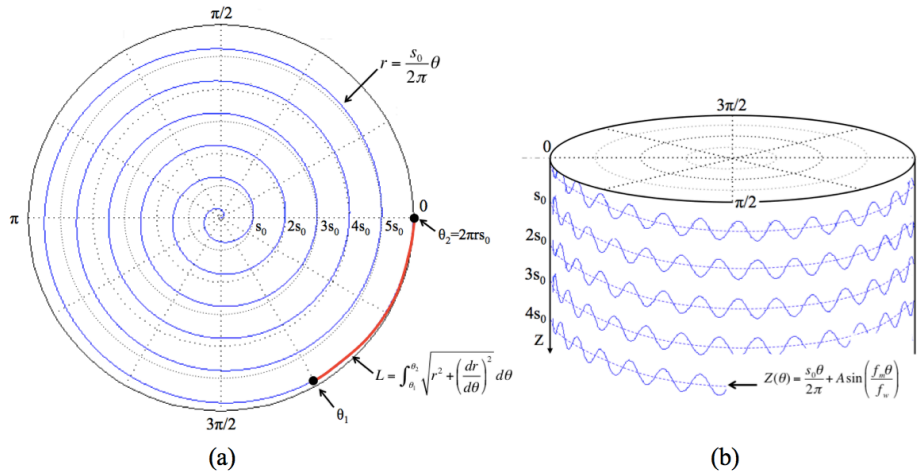


Figure 9. Tool motions in (a) plunging-type texturing (facing) and (b) sliding-type texturing (turning).

In the case of constant angular frequency (i.e., constant f_w), $d\theta/dt$ is constant and the relative phase angle between successive machining passes [9, 10] is given by Eq. (2),

$$\varphi = \left(\frac{f_m}{f_w} - \text{INT} \left(\frac{f_m}{f_w} \right) \right) * 2\pi \quad \text{Eq. (2)}$$

In Eq. (2), in-phase modulation conditions correspond to $\varphi = n*2\pi$ and out-of-phase modulation conditions correspond to $\varphi = (2n+1)\pi$, where n is zero or a non-zero integer. Intermediate phase differences result for other values of φ . For constant angular frequency, a relationship between tool position (r , θ , z) and time t is relatively straightforward. Constant surface speed configurations are important for facing-type machining configurations as such conditions provide for uniform material removal conditions (e.g., cutting velocity) and also yield surface textures of constant size, as is shown in the ensuing. In this case, $d\theta/dt$ is time-varying to maintain constant v_0 and the distance traveled along the spiral must be considered. The path length for a given angular traverse (i.e., to position θ_1) is given by the arc length of the spiral in Eq. (3),

$$L(\theta) = \int_{\theta_1}^{\theta_2} \sqrt{r^2 + \left(\frac{dr}{d\theta} \right)^2} d\theta = \frac{s_0}{2*\pi} \int_{\theta_1}^{2\pi R/s_0} \sqrt{\theta^2 + 1} d\theta \quad \text{Eq. (3)}$$

where $\theta_2 = 2\pi R/s_0$ is the angular position (i.e., number of spiral turns) at the periphery of the workpiece face and R is the radius of the workpiece (Fig. 9). At constant surface speed, the tool velocity along the spiral is constant at v_0 and it can be shown that the time t is given by the path length in Eq. (3) divided by the cutting velocity as in Eq. (4),

$$t(\theta) = \frac{s_0}{2*\pi*v_0} \int_{\theta_1}^{2\pi R/s_0} \sqrt{\theta^2 + 1} d\theta \quad \text{Eq. (4)}$$

This expression for the relationship between θ and t in Eq. (4) can be used to provide the axial position of the tool relative to the workpiece as a function of angular position θ . The motion of the tool in the axial direction (Z -direction) is given by $Z=A\sin(\omega t)$. Given the effect of a general offset c , as described in the preceding section, the axial position is modified as in Eq. (5),

$$Z(t) = A(c + \sin(2 * \pi * f_m * t)) \quad \text{Eq. (5)}$$

Substitution of Eq. (4) in Eq. (5) provides the position of the tool apex in polar coordinates (r , θ , z) as a function of time t and the controllable process parameters (f_m , A , s_0) and is provided in Eq. (6),

$$Z(\theta) = A(c + \sin\left(\frac{s_0*f_m}{v_0} \int_{\theta_1}^{2\pi R/s_0} \sqrt{\theta^2 + 1} d\theta\right)) \quad \text{Eq. (6)}$$

While Eq. (6) describes the relative tool position in time, the actual shape left by the tool interaction with the work surface is modeled by determining the relative intersection between the work surface and the corresponding tool geometry along this path. In this case, the tool geometry can be modeled ideally as a circle or sphere of radius R_t whose instantaneous position is defined by Eq. (6). Boolean subtraction of this shape from the work surface can be implemented numerically.

A similar geometric model can be developed for sliding-type texturing. In turning configurations, the motion of the tool takes on a helical path across the outer diameter of the workpiece at a

constant radial position (i.e., r is constant) and within θ - Z space as in Fig. 9(b). At constant spindle frequency (i.e., f_w is constant), the angular location of the tool is defined by Eq. (7),

$$\theta(t) = 2 * \pi * f_w * t \quad \text{Eq. (7)}$$

Tool motion in the axial direction (i.e., Z -direction) is given by the instantaneous feed of the tool and the superimposed modulation $A \sin(\omega t)$ as in Eq. (8); substitution of Eq. (7) yields an expression in terms of angular location in Eq. (9),

$$Z(t) = s_0 * f_w * t + A * \sin(2 * \pi * f_m * t) \quad \text{Eq. (8)}$$

$$Z(\theta) = \frac{s_0 * \theta}{2 * \pi} + A * \sin\left(\frac{f_m * \theta}{f_w}\right) \quad \text{Eq. (9)}$$

Eq. (9) and a constant value for the radial coordinate describe the relative tool position. The shape of the work surface is determined by solving for the intersection with the corresponding tool geometry along this path.

5.2.2 Micro-Textured Surface Generation

A CNC lathe was retrofitted with an electro-mechanical tool holder (M4 Sciences) that facilitated controlled tool motions superimposed on the machine feed in the axial direction of the workpiece, as shown in Fig. 10(a). A polycrystalline (PCD) diamond insert (Hertel HT-420CD) with a nose radius of 0.8 mm was used for finishing the work surface. A carbide grooving insert (Iscar MIFR 8-1.60-0.8) with a nose radius of 0.8 mm was used for the plunging-type texturing experiments and a carbide threading insert (Iscar MITR 8-MT1-0.05) with a nose radius of 0.05 mm was used for sliding-type texturing; both were held in a boring bar (Iscar MG08-STFPR-09X) attached to the electro-mechanical tool holder. Tool offsets were determined by white light interferometry (Zygo) of conventionally grooved workpiece samples. The sinusoidal waveform (voltage, frequency) to the piezoelectric actuator was provided using an electric controller/amplifier (M4 Sciences). Tool displacement was monitored using a capacitance probe (Capacitac). Micro-scale surface features were characterized using optical microscopy and white light interferometry. A Nikon stereoscope (SMZ800) was used to scan the surface while a white light interferometer was used to measure the three-dimensional character of the surface features.

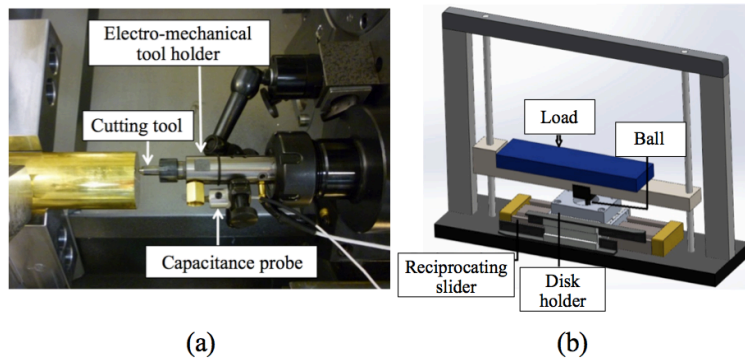


Figure 10. (a) Experimental machining setup and (b) ball-on-flat wear test configuration.

5.2.3 Wear Testing and Coupled Microstructure Response

Wear experiments were carried out using a ball-on-flat reciprocating test machine, as depicted in Fig. 10(b). Textured and non-textured (control) disks were tested against AISI 440C stainless steel balls of 3 mm radius and 690 HV hardness. The sliding time (20 min), amplitude (10.5 mm), frequency (1.5 Hz) and normal load (34 N) were kept constant for all wear tests. 2 mL of a

synthetic poly-alpha-olefin oil (Synton PAO 40) were applied on the surfaces prior to each test and no additional lubricant was added during the tests. Wear performance was obtained after three tests under the same condition. Volume loss (V_f) was determined by image analysis after 45 wear track width (W_f) measurements for each test. Subsurface microstructure was characterized using electron backscatter diffraction (EBSD) with a Tescan Mira3 XM FEG-SEM and TSL OIM analysis software to obtain crystallographic orientation information. Samples for EBSD were prepared using standard mechanical polishing methods.

The effect of a distribution of dimple textures on wear performance was measured. Initial untextured brass and aluminum alloy surfaces were produced with roughness $R_a < 0.150 \mu\text{m}$. Textured surfaces were then produced using these workpieces at constant spindle speed of $v_0 = 0.9 \text{ m/min}$, modulation frequency of $f_m = 100 \text{ Hz}$ and modulation amplitude of $A=0.015 \text{ mm}$. Figure 11 shows optical and interferometric images of the plunging type textures produced in the brass and aluminum workpieces. From the figure, the dimples have uniform geometry with no discernable differences observed between the work materials. Table 1 summarizes the dimple depth measurements obtained from interferometry. From the table, the direct-write texturing process was capable of generating dimples with sub-micron errors in depth that may be caused by deformation and/or machine-tool compliance. Further, the surface profilometry in Fig. 11 reveals a negligible region of material pile-up at the tool exit.

Table 1. Experimental surface texturing conditions and measurements for wear tests.

Initial Conditions			Surface Texturing Conditions					Surface Texture Measurements		
Sample	Material	R_a (μm)	f_m (Hz)	A (mm)	C	s_0 (mm/rev)	V_0 (m/min)	Target dimple depth (mm)	Actual dimple depth (mm)	Actual depth error (μm)
CS	Brass 360	0.137								
CS	AA6061-T6	0.121								
TS	Brass 360	0.143	100	0.015	0	1.5	0.9	0.01500	0.01492	0.08
TS	AA6061-T6	0.100	100	0.015	0	1.5	0.9	0.01500	0.01439	0.61

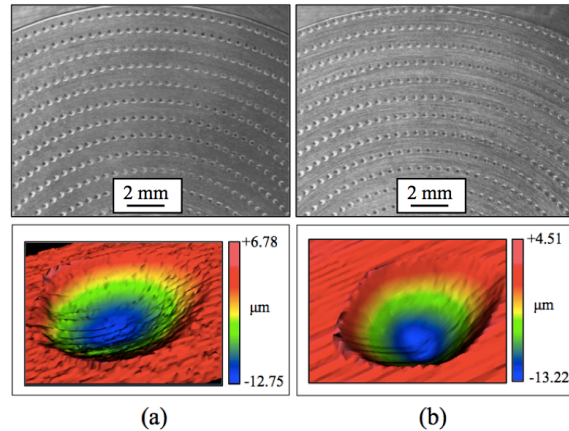


Figure 11. Surfaces created by plunging-type texturing in (a) brass 360 and (b) AA6061-T6 at $A = 0.02 \text{ mm}$, $r_t = 2.5 \text{ mm}$, $d = 0 \text{ mm}$, $v_0 = 12 \text{ m/min}$, $s_0 = 2.0 \text{ mm/rev}$ and $f_m = 100 \text{ Hz}$.

Tribological wear tests were carried out for both untextured control surfaces (CS) and textured surfaces (TS) and the results are summarized in Fig. 12. Under the experimental conditions studied, textured surfaces reduced wear with respect to the untextured control surfaces on both materials. A wear reduction of 32% and 25% was achieved by texturing the surfaces of the brass and the aluminium, respectively. Figure 12 shows representative wear track profiles on the textured and untextured samples. From the figure, it can be seen that the wear profiles on samples without the surface textures were wider and deeper than those on textured surfaces. As can also

be seen in Fig. 12(a), the amount of material plastically deformed at the edges of the wear track was also reduced for the textured brass samples.

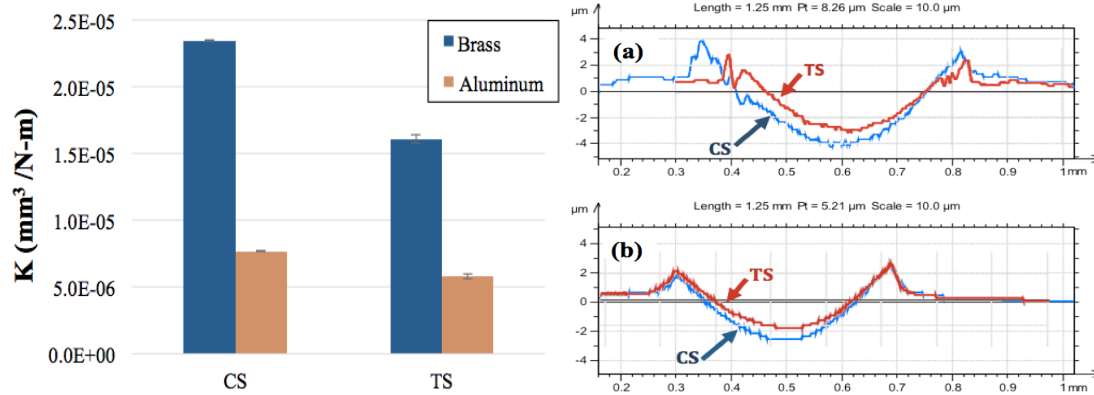


Figure 12. Wear factor measurements (left) for control surface samples and textured surface samples in brass and aluminum. Wear track profiles (right) on textured (TS) and untextured (CS) samples.

It is well known that conventional machining can induce grain refinement and phase transformations in the work subsurface arising from severe plastic deformation that occurs during the chip formation process [11, 12]. It has been shown elsewhere [13] that machining parameters of undeformed chip thickness and rake angle have primary influence on spatial extent and severity of the deformation in the work surface, respectively. In plunging-type texturing configurations, these parameters vary continuously throughout the surface generation process. To understand the effects of the plunging-type surface texturing process on surface and subsurface integrity, a controlled experiment was conducted to characterize the microstructure underneath a model dimple-type surface texture. Sinusoidal topographical features were created with a high-speed steel tool with a rake angle of $\alpha = 0^\circ$, the modulation amplitude was $A = 0.010$ mm and the modulation frequency was restricted to $f_m = 1$ Hz to facilitate imaging of microstructure using OIM in EBSD. The resulting aspect ratio of the surface textures (i.e., $2A/\lambda$) was 0.2.

The microstructure in the textured subsurface is provided in Fig. 13. From the figure, the subsurface microstructure featured spatial gradation in terms of grain size, width of the severely sheared zone and crystallographic texture. Broadly, this gradation involved a saturated microstructure field featuring an equiaxed ultra-fine grained (UFG) morphology on the exit side of the sinusoidal tool motion and a clearly microcrystalline structure on the entry side of the sinusoidal motion. The extent of the microstructure refinement can be quantified by identifying grains exhibiting high-angle misorientation, generally in excess of 15° . The average grain diameter where grain boundaries exceed this threshold was measured using the line intercept method and is given by δ_{15° in the ensuing. For the exit side of the sinusoidal tool motion (left in Fig. 13), the microstructure could be characterized by $\delta_{15^\circ} = 0.5 \mu\text{m}$ over a thickness of $5 \mu\text{m}$ in the subsurface. This can be compared to the entry side of the sinusoidal tool motion (right in Fig. 13) where $\delta_{15^\circ} > 2 \mu\text{m}$ is observed to exist over the subsurface depth. In this regard, an asymmetric microstructure field comprising of UFG domains on the exit side and coarse grains on the entry side of the surface texture is symptomatic of severe shear strains being imposed in the former [14]. Crystallographic textures on the topographically textured surfaces were extracted from these OIM graphs and revealed a similar character as that seen in conventional orthogonal machining with constant s_0 . Texture in conventional machined surfaces involves concentration of crystallographic orientations along 3 distinct fibers attributable to simple shear and rolling-type deformation geometries [15]. However, strengths of zones within these fibers were seen to vary periodically with s_0 during topographic texturing.

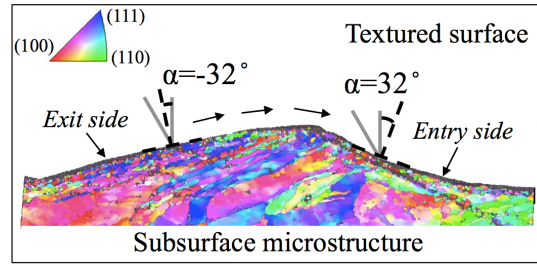


Figure 13. Subsurface microstructure and texture in topographical surface texturing.

The gradation of microstructure in Fig. 13 is a consequence of the periodically varying effective rake angle $\alpha_{\text{eff}}(t)$ that manifests in variable strains and depths of severely sheared zones under the generated surface [13]. The effective rake angle assumes a strongly negative value in the exit face of the tool at $\alpha_{\text{eff}} = -32^\circ$ and an equivalent positive value during entry of the tool at $\alpha_{\text{eff}} = 32^\circ$. From previous investigations [15, 16], it is clear that variation in α from -32° to 32° can have profound implications on deformation and corresponding microstructural response in the work subsurface.

6. Future Studies and Implementation on Continuous Processing Systems

The above results in development of integrated severe surface plastic deformation (S^2PD) and modulation-assisted texturing (MAT) platforms provide a first-pass attempt to link microstructure and texture predictive capability in FE formulations coupled with the VPSC framework. From the results, wear resistance of textured surfaces and texture evolution within surface severely deformed surfaces can be obtained by a calibrated empirical model of wear given an initial surface state / condition. Calibration of the FE model and the VPSC parameters was enabled by high-resolution *in situ* digital image correlation, as well as empirical measurements of the as-deformed microstructure (and texture) in a unit model impression process. Extension of the unit process in the FE model enabled prediction of deformation in surface mechanical attrition. Coupled effects on grain refinement introduced by the texturing process, observed using electron microscopy and explained due to spatially-varying processing parameters, must be accounted for in the generation of the final surface by the hybrid S^2PD and MAT processing route.

Toward developing a fully-functional surface modeling capability to determine optimal multi-scale textured surfaces for performance applications, the integrated modeling capability developed in the course of the present study must be linked with *calibrated* predictive tools for microstructure variables beyond that developed here for crystallographic texture (e.g., grain size, phase transformations, twinning) wherein the deformation conditions in both the microstructure surface generation and texturing process can be used to elucidate the final surface state. A potential approach to a more expansive surface modeling capability for multi-scale textured surfaces could be found in leveraging the present models/codes with extant process-microstructure (and performance) libraries to provide first pass estimation of microstructure characteristics based on the wealth of information regarding grain refinement mechanisms in bulk SPD studies. Expansive literature on grain refinement mechanisms in bulk SPD provide a potentially attractive resource in this regard and will be used in future studies to establish surface performance models of significantly higher fidelity and overall utility. The ultimate goal of this area of research is to facilitate predictive tools to *a priori* determine processing configurations needed to generate plastically graded component surfaces with custom-tailored microstructures (e.g., twinned, bimodal) and mechanical properties.

7. Publications Resulting From this Project

1. R. Gandhi, D. Sebastian, S. Basu, J. B. Mann, P. Iglesias, C. Saldana, "Surfaces by vibration/modulation-assisted texturing for tribological applications", *submitted*.
2. S. Basu, Z. Wang, C. Saldana, "Texture evolution in severe surface plastic deformation," *submission June 2015*.
3. Z. Wang, S. Basu, T. G. Murthy, C. Saldana, "Calibrated expanding cavity solution for surface deformation processing," *submission June 2015*.
4. S. Basu, Z. Wang, C. Saldana, "Subsurface deformation in surface mechanical attrition processes," Proceedings of the ASME Manufacturing Science and Engineering Conference, June 2015.
5. Z. Wang, S. Basu, C. Saldana, "Crystallographic textures produced during sand blasting," Proceedings of the ASME Manufacturing Science and Engineering Conference, June 2015.

8. Bibliography

1. F. Du, S. Yadav, C. Moreno, T. G. Murthy, C. Saldana, "Incipient straining in severe plastic deformation methods," *Journal of Materials Research*, 2014, Vol. 29, pp. 718-728.
2. R. Lebensohn and C. Tome, "A self-consistent anisotropic approach for the simulation of plastic deformation and texture development of polycrystals: Application to zirconium alloys," *Acta Metallurgica et Materialia*, Vol. 41, pp. 2611-2624, 1993.
3. S. Basu and M. R. Shankar, "Crystallographic textures resulting from severe shear deformation in machining," *Metall. Mater. Trans. A*, Vol. 46, no. 2, pp. 801-812.
4. W. F. Hosford, *The mechanics of crystals and textured polycrystals*, Oxford Press, 1993.
5. S. Abolghasem, S. Basu and M. R. Shankar, "Quantifying the progression of dynamic recrystallization in severe shear deformation at high strain rates," *Journal of Materials Research*, 28, pp. 2056-2069, 2013.
6. Y. Guo, C. Saldana, W. D. Compton, and S. Chandrasekar, "Controlling deformation and microstructure on machined surfaces," *Acta Mater.*, Vol. 59, no. 11, pp. 4538-4547, 2011.
7. I. J. Beyerlein, C. N. Tomé, "Modeling transients in the mechanical response of copper due to strain path changes," *International Journal of Plasticity*, Vol. 23, Pages 640-664, 2007.
8. S. Sabbaghianrad, J. Wongsan-Ngam, M. Kawasaki, T. G. Langdon, "An examination of the saturation microstructures achieved in ultrafine-grained metals processed by high-pressure torsion," *Journal of Materials Research and Technology*, Vol. 3, Pages 319-326, 2014.
9. J. B. Mann, Y. Guo, C. Saldana, W. D. Compton, S. Chandrasekar, "Enhancing material removal processes using modulation-assisted machining," *Trib. Int.*, 44, 1225-1235, 2011.
10. D. E. Brehl and T. A. Dow, "Review of vibration-assisted machining," *Precis. Eng.*, Vol. 32, pp. 153-172, 2008.
11. M. C. Shaw, *Metal Cutting Principles*, Second Edition, Oxford: Clarendon Press, 1984.
12. T. L. Brown, C. Saldana, T. G. Murthy, J. B. Mann, Y. Guo, L. F. Allard, A. H. King, W. D. Compton, K. P. Trumble, and S. Chandrasekar, "A study of the interactive effects of strain, strain rate and temperature in severe plastic deformation of copper," *Acta Mater.*, Vol. 57, pp. 5491-5500, 2009.
13. Y. Guo, C. Saldana, J. B. Mann, R. M'Saoubi, S. Chandrasekar. "Deformation and microstructure in machining," *Advanced Materials Research* 223, pp. 325-331, 2011.
14. F. A. Mohamed and S. S. Dheda. "On the minimum grain size obtainable by equal channel angular pressing." *Materials Science and Engineering A* 580, pp. 227-230, 2013
15. S. Basu, S. Abolghasem, M. R. Shankar. "Mechanics of intermittent plasticity punctuated by fracture during shear deformation of Mg alloys at near-ambient temperatures," *Metallurgical and Materials Transactions A* 44, pp. 4558-4566, 2013
16. S. Abolghasem, S. Basu, S. Shekhar, J. Cai, and M. R. Shankar, "Mapping subgrain sizes resulting from severe simple shear deformation," *Acta Mater.*, vol. 60, pp. 376-386, 2012.